

## Article

# Impacts of Surface Deformation Induced by Underground Mining of Metal Mines on Above-Ground Structures: A Case Study

Peizheng Liu <sup>1,2,3</sup>, Hui Li <sup>2,3</sup>, Leiming Wang <sup>1,2,3,4,5,\*</sup>  and Shenghua Yin <sup>2,3</sup>

<sup>1</sup> Sinosteel Maanshan General Institute, Mining Research Co., Ltd., State Key Laboratory Safety and Health for Metal Mines, Maanshan 243000, China; d202110052@xs.ustb.edu.cn

<sup>2</sup> School of Civil and Environment Engineering, University of Science and Technology Beijing, Beijing 100083, China; lihuimiracle@163.com (H.L.); ustb\_ysh@163.com (S.Y.)

<sup>3</sup> Key Laboratory of High-Efficient Mining and Safety of Metal, Ministry of Education, University of Science and Technology Beijing, Beijing 100083, China

<sup>4</sup> State Key Laboratory of Coal Mine Resources and Safety Mining, China University of Mining and Technology, Xuzhou 221116, China

<sup>5</sup> Key Laboratory of Green Chemical Engineering Process, Ministry of Education, Wuhan Technological University, Wuhan 430205, China

\* Correspondence: ustb\_wlm@126.com; Tel.: +86-15201452103

**Abstract:** The surface deformation caused by underground mining seriously affects the normal life and personal safety of local residents and also causes unfavorable factors for the safe and efficient exploitation of underground resources. While the study of surface deformation caused by underground mining of metal mines requires a large amount of measured data as support, the measured data is particularly scarce, which severely hinders the study of surface deformation caused by underground mining. In this paper, in order to study the impact of underground mining on surface structures in metal mines, we take the Fu Lao Zhuang Iron Mine in Anhui Province, China, as the research object and put forward a comprehensive measurement method based on the flat plate beam theory. Using empirical formulas combined with the methods of thickness-to-span ratio and the relaxation coefficient, etc., we carry out numerical simulation calculations for the displacement of the surface triggered by the mining of the ore body by using FLAC3D software. We calculate the maximum inclination deformation, curvature, and horizontal deformation values of the ground surface by referring to the displacement and deformation with reference to the displacement and deformation formula; the maximum tilt deformation, curvature, and horizontal deformation values of the ground surface are calculated, and finally, the permissible values of the design specifications are combined to make a judgment. The research results of this paper put forward the prerequisite for improving the surface deformation induced by underground mining.

**Keywords:** underground mining; surface deformation; structures deformation; FLAC<sup>3D</sup> software; modeling



**Citation:** Liu, P.; Li, H.; Wang, L.; Yin, S. Impacts of Surface Deformation Induced by Underground Mining of Metal Mines on Above-Ground Structures: A Case Study. *Minerals* **2023**, *13*, 1510. <https://doi.org/10.3390/min13121510>

Academic Editor: Abbas Taheri

Received: 6 September 2023

Revised: 20 November 2023

Accepted: 24 November 2023

Published: 30 November 2023



**Copyright:** © 2023 by the authors. Licensee MDPI, Basel, Switzerland. This article is an open access article distributed under the terms and conditions of the Creative Commons Attribution (CC BY) license (<https://creativecommons.org/licenses/by/4.0/>).

## 1. Introduction

Underground mining damages underground rock mass and breaks the original equilibrium state of the in situ stress of underground rock. A little underground mining disturbance has little influence on the surface [1]. However, with the continuous mining of mine resources, the underground resources are constantly increased, resulting in the increasing scope of underground goaf, which leads to the redistribution of stress in the surrounding rock of the roadway and may cause surface deformation [2]. In severe cases, it may induce the collapse of surface structures and other serious consequences [3].

The surface deformation caused by underground mining is a very complicated process, which has been predicted by some scholars. The research community has discussed various

assessment and prediction techniques used to study surface deformation and environmental impact caused by underground mining [4]. Cui et al. studied the prediction method of surface deformation and analyzed the relationship between the top Angle and coal seam dip Angle [5]. A new Angle expression of the top Angle or maximum subsidence position is established, which can easily determine the maximum subsidence position of the surface, avoid the malpractice of systematizing the inclination Angle of coal seam artificially, and ensure the natural continuity of the inclination Angle of coal seam. The subsidence prediction model is proposed, and the characteristics of the subsidence basin are analyzed [6]. However, this method cannot be applied to the prediction of steep or vertical coal seam mining at present because of its complex movement mechanism and discontinuous deformation. Based on rock rheology theory, Li et al. established a theoretical model for the prediction and analysis of dynamic settlement in deep underground mining and put forward a formula that can be used to predict surface movement caused by deep pillarless sublevel caving [7]. Marian Maeschalko et al. studied the problem of slope movement induced by underground mining activities and analyzed the effect of mining activities on slope deformation, using three different methods to study different cases of slope deformation, and found that the positioning of inclinometers measurement in the active portion and nearby boreholes is very important [8,9]. Pan et al. established a new model that can identify the beginning of the subcritical settlement in deep pillar-free mining and established an L-shaped PKS model based on the elastic plate theory to determine the critical span of PKS failure and identify the subcritical settlement in pillar-free mining, providing a new idea for the surface settlement control design in pillar-free mining [10]. Yang et al. studied the influence of surface settlement caused by underground mining on slope stability conditions, used InSAR technology and temporal and spatial statistics of landslide cracks to study the slow subsidence and expansion process caused by underground mining, and studied the clustering phenomenon of landslide and crack under the action of subsidence [11]. Li et al. carried out a numerical simulation of roof deformation and surface subsidence under the three methods of caving mining, room and pillar mining, and cement backfill mining, and found that the amount of roof and surface subsidence decreases sequentially, and the caving mining and room and pillar mining disturb the open pit slopes significantly for the shallow ore body, while the cement backfill mining can utilize the mined-out waste as the backfill material. The effect of the back mining process on the roof and surface is small, and the control effect on the stability of the slope is better [12]. Xia et al. utilized the D-InSAR technology for mining subsidence monitoring to accurately detect illegal mining activities. By integrating GIS technology, they established a spatial-temporal relationship model between surface deformation and underground mining subsidence characteristics, resulting in the development of a rapid, efficient, and precise method for identifying surface subsidence that can yield better results [13]. The serious tunnel cracks caused by underground mining of coal mines were investigated by Li et al. The parameters were analyzed, the tunnel settlement was calculated, and the radial deformation of the roadway caused by underground mining of coal mines was evaluated using the PIM method. Additionally, a grouting method was proposed to reduce the deformation of old goaf under the tunnel [14]. The study is helpful in elucidating the temporal and spatial evolution of slow subsidence in mining areas and its influence on loess landslides. Zeng et al. studied mining subsidence based on rheology and established an important relationship between the time factor and the rheological parameters of rock mass by using the viscoelastic theory and corresponding principle [15]. Zhang et al. proposed a geometric and local adaptive grid-based FDM modeling method for large surface deformation in underground mining, analyzed the surface deformation of the Yanqianshan Iron mine, and used this method to conduct a numerical study of Liaoning Province, China, and compared the numerical results with DEM simulation [16]. The method has been applied to the prediction of surface subsidence in Anjialing No.1 underground mine in Shanxi Province. Takashi Sasaoka et al. [17] discussed the surface subsidence behavior caused by longwall mining based on the measured data of coal measure strata in Balikpapan, Indonesia, and

used the measured data for settlement analysis and prediction, which should be applied to local strata and mining conditions worldwide. Zhao et al. conducted an estimation of roadway stability and surface deformation resulting from the conversion of open-pit mining to underground mining. They developed three-dimensional finite difference numerical models for surface landforms, orebody, and faults, which were then calibrated using satellite monitoring data on surface tailings at multiple locations [18]. Carolina Brucker et al. [19] discussed the surface subsidence caused by underground mining and its potential risks to underground space planning.

All of the aforementioned studies primarily focus on surface subsidence resulting from underground mining, with most of them specifically examining coal mines. However, there is a lack of research on surface deformation caused by underground mining in non-coal or metal mines [20]. There are significant differences between coal and non-coal mines. Firstly, their formation processes differ; coal is formed through biochemical and physicochemical processes from plant remains, resulting in sedimentary organic minerals that consist of various polymer compounds and minerals. On the other hand, non-coal deposits are formed through the migration and enrichment of chemical elements in the crust under mineralization processes. Mineralization refers to the geological process where useful components separate from other components in the crust and concentrate to form deposits. In simpler terms, ore-forming materials for non-coal deposits originate from within the crust itself. Additionally, there are substantial differences in internal stress intensity between coal and non-coal ore bodies due to these distinct mineralization processes; specifically, coal ore bodies have lower stress intensity compared to non-coal ore bodies. Secondly, mining methods also vary between these two types of mines at different stages; however, this paper does not discuss the diverse range of mining methods used for non-coal deposits.

This paper conducts a comprehensive study on how underground mining affects surface structures in metal mines. The Fulaozhuang Iron Mine, located in Anhui Province, China, serves as our research subject. We employ various numerical simulation techniques such as the thick-span ratio method, loose coefficient method, slab beam theory, and K.B. Lu Peinie empirical formulas along with FLAC3D software to calculate displacement generated by ore body extraction accurately.

## 2. Materials and Methods

### 2.1. Mechanical Experiment and Reconstruction Method

(1) Mining status: calculation and analysis of mining conditions in recent years, shown in Figure 1;

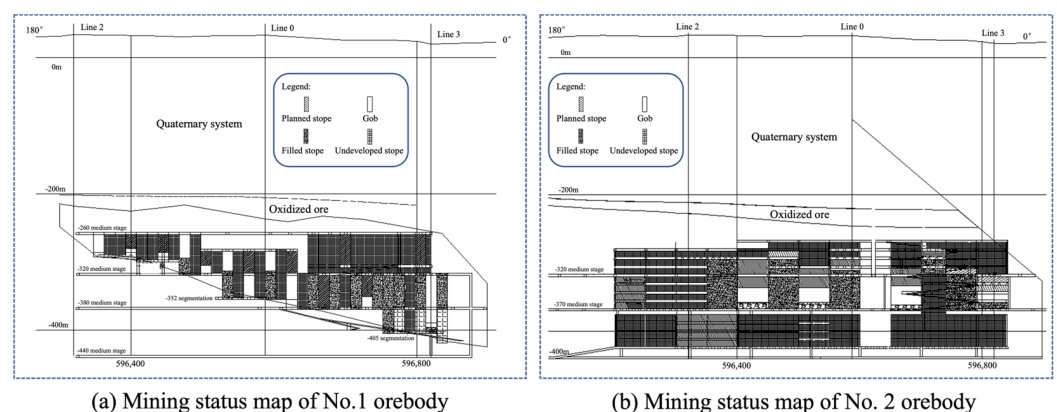


**Figure 1.** Mining status map of No. 1 (a) and No. 2 (b) orebodies.

(2) The mining end of the lower middle section: No. I orebody corresponds to the  $-405$  m sub-section, No. II orebody corresponds to the  $-425$  m sub-section, and now it is unified to the  $-425$  m sub-section;

(3) The mining end of the middle section: No. I orebody corresponds to the  $-352$  m and  $-380$  m sections, and No. II orebody corresponds to the  $-380$  m sections, which are now unified as  $-380$  m sections;

(4) The mining end of the upper middle section: the No. I orebody corresponds to the  $-300$  m and  $-320$  m sections, and the No. II orebody corresponds to the  $-320$  m sections, which are now unified as  $-320$  m sections.

No. I orebody adopts the downward large-hole open stope mining with subsequent filling mining method, shown in Figure 1a. The stope is arranged perpendicular to the strike of the orebody, the stope span is 15 m, and the stope length is the thickness of the orebody. The mining range is between Line 3 in the north and Line 2 in the south. Basically, line 0 is used as the boundary, and the orebody between line 0 and line 3 has a good tendency to extend. According to the different elevations of the floor of the orebody, two mining sections are divided, namely the  $-308$  m section and the  $-380$  m section (or  $-405$  m section). Between line 0 and line 2, the mining is divided into a single section,  $-300$  m section,  $-320$  m section, or  $-352$  m section.

No. II orebody selects sublevel open stope mining with the subsequent filling mining method, shown in Figure 1b. The ore room is arranged along the strike of the orebody. The stope is 50 m long, and the stope span is the thickness of the orebody. The mining range is 130 m south of the 3rd line in the north to the 2nd line in the south, and the II orebody extends well in strike and tendency. It is divided into  $-425$  m sections,  $-380$  m sections, and  $-320$  m sections.

Next, we collect the mine exploration, exploitation, mining permits, measured data, field surveys, and statistics of rock joints and cracks, and combine them with field rock sampling to carry out laboratory mechanical tests. In the  $-320$  m middle section of the Fulaozhuang Iron Mine, the occurrence, scale, density, shape, and groundwater status of the structural plane in the orebody and roof and floor rock mass are investigated. We collect mine samples, carry out laboratory mechanical experiments and experimental analysis, and use FLAC<sup>3D</sup> 3.0 simulation software (ITASCA International Inc., Minneapolis, Minnesota, USA) to carry out the three-dimensional reconstruction.

## 2.2. Laboratory Experiment-Determination of Reconstruction Parameters

After sampling the ore body and rocks of the roof and floor of the iron mine, an indoor rock mechanics experiment was carried out. A WEP-600 microcomputer-controlled screen display universal testing machine and shear strength testing machine (Jinan Star Testing Technology Co, Ltd, Jinan, China) were used in the experiment, shown in Figure 2. The experimental results are shown in Table 1, and the result is the average value of the test results of the sample:

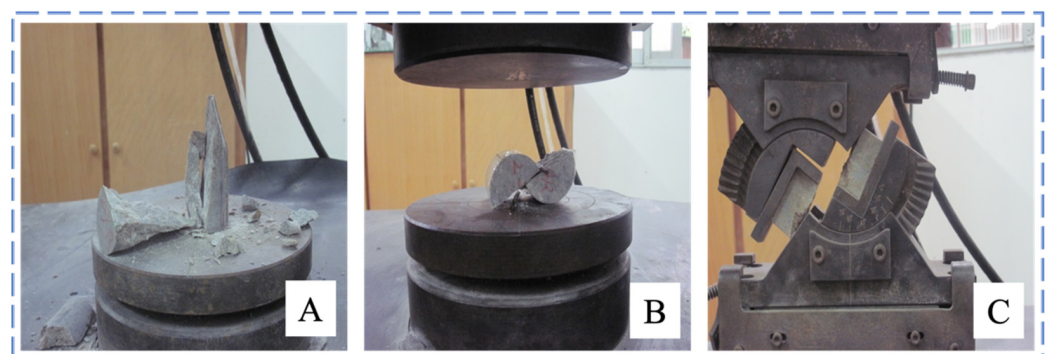


**Figure 2.** Rock compression test (A), rock tensile test (splitting method) (B), and rock shear test (C).

**Table 1.** Summary table of physical and mechanical parameters of rocks.

Lithology	Density (g/cm <sup>3</sup> )	Tensile Strength (MPa)	Compressive Strength (MPa)	Elasticity Modulus (GPa)	Poisson Ratio	Cohesion (MPa)	Internal Friction Angle (°)
Gneiss	2.79	4.12	81.00	50.8	0.26	10.48	44.76
Marble	2.72	5.57	99.67	67.7	0.32	8.04	44.00
Orebody	3.32	4.32	111.83	54.2	0.28	11.68	46.61

## (1) Experiment content

Physical and mechanical parameters of the sampled ore rock were tested, including physical properties of the ore rock experiment, uniaxial compressive strength experiment, splitting tensile experiment, shear deformation experiment, and deformation experiment.

## (2) Mechanical parameter test

## ① Physical mechanics experiment-Density test

Three samples are prepared in each group by means of the measurement method. They are rectangular regular samples, and the samples are in the state of air drying. Use the following formula to calculate:

$$\rho_d = \frac{m_d}{A \times H} \quad (1)$$

where:  $\rho_d$ —rock density (g/cm<sup>3</sup>);  $m_d$ —sample weight (g);  $A$ —mean area (cm<sup>2</sup>);  $H$ —mean height (cm).

## ② Uniaxial compression test

Objective: To measure the compressive strength, elastic modulus, and Poisson's ratio of rock. In detail, the loading speed is 4 mm/800 s; adopt the load parameter is 5 kN/grid; the displacement parameter is 0.02 mm/grid; the uniaxial compressive strength of rock is calculated according to the following:

$$R = \frac{P}{A} \times 10 \quad (2)$$

where:  $R$ —Uniaxial compressive strength of rock, MPa;  $P$ —Maximum damage load, kN;  $A$ —The cross-sectional area of the sample perpendicular to the loading direction, cm<sup>2</sup>.

## ③ Splitting tensile test

Objective: To measure the tensile strength of rock. The specification: Diameter × height = 50 mm × 50 mm; the loading speed is 5 mm/50 s; The following formula is used to calculate the tensile strength of rock:

$$\sigma_t = \frac{2 \times P}{\pi \times d \times h} \quad (3)$$

where:  $\sigma_t$ —Tensile strength of rock, (MPa);  $P$ —Maximum load at the time of failure, (kN);  $d$ —Diameter of the rock sample (cm);  $h$ —The height of the rock sample, (cm).

## ④ Shear test

Objective: The shear strength, cohesion, and internal friction angle of the rock were measured. The specification: Length × width × height = 50 mm × 50 mm × 50 mm; the loading speed: 5 mm/50 s; the load parameter: 5 kN/grid. The normal stress and shear stress on the shear plane of the specimen are calculated according to the following formula respectively:

$$\sigma = \frac{P \times (\cos \alpha + f \times \sin \alpha)}{B \times H} \times 10 \quad (4)$$

$$\tau = \frac{P \times (\sin \alpha + f \times \cos \alpha)}{B \times H} \times 10 \quad (5)$$

where:  $P$ —The axial pressure of rock failure, kN;  $B, H$ —The width and height of the block, cm;  $\alpha$ —Clamp shear angle, degree;  $f$ —Friction coefficient of the roller,  $f = 0$ .

According to the  $\sigma$  and  $\tau$  values of each group of samples, the shear strength  $c$  and  $\varphi$  of regular rock blocks are calculated by the least square estimation method.

⑤ Deformation test

The rock deformation test measures the longitudinal and transverse deformation of the sample under the action of longitudinal pressure and then calculates the elastic modulus and Poisson’s ratio of the rock.

Four samples were prepared in each group; the sample size was  $5 \times 5 \times 10$  cm, and the height-to-diameter ratio was 2:1. The sample of rock uniaxial deformation test is saturated. The elastic modulus and Poisson’s ratio are calculated as follows:

$$E = \frac{\sigma_{50}}{\varepsilon_{h50}} \tag{6}$$

$$\mu = \frac{\varepsilon_{d50}}{\varepsilon_{h50}} \tag{7}$$

where:  $E, \mu$ —Elastic modulus (MPa) and Poisson’s ratio;  $\sigma_{50}$ —Equal to 50% compressive strength stress value, MPa;  $\varepsilon_{d50}$ —The longitudinal strain value at  $\sigma_{50}$ ;  $\varepsilon_{h50}$ —The transverse  $\sigma_{50}$  strain value at  $\sigma_{50}$ .

The compressive strength of the backfill (cement–sand ratio 1:12) was tested using the TSY-300 pressure testing machine, and the test results are shown in Table 2.

**Table 2.** Compressive strength test results of backfill.

No.	Actual Age Period (Day)	Sample Specifications (mm)	Compression Area (mm <sup>2</sup> )	Single Block Load (kN)	Single Block Strength (MPa)	Representative Strength Value (MPa)
1	28	70.7 × 70.7 × 70.7	5000	10.5	2.8	3.1
2	28		5000	11.3	3.1	
3	28		5000	12.4	3.3	
1	28		5000	12.3	3.3	3.7
2	28		5000	13.6	3.7	
3	28		5000	14.7	4.0	

2.3. Modeling and Calculation Condition Setup via Flac<sup>3D</sup>

According to the distribution of ore bodies, the upper boundary of the model is the mining surface, and the other boundaries are the mining size, about three times the self-mining boundary. Namely: the north–south direction length is 960 m, from 3,596,070 m to 3,597,030 m; the east–west width is 700 m, from 402,900 m to 403,600 m; The lower boundary is −600 m. The model is divided into 52,951 nodes and 263,296 units.

(1) Boundary conditions. In numerical simulation, some boundary conditions are applied to replace the original medium outside the model affected by mining. In this calculation model, free constraints are applied to the upper surface boundary, fixed constraints are applied to the bottom surface, and hinge constraints are applied to the X and Y direction boundary. This study adopts the Mohr–Coulomb constitutive model. The theory of plastic increment assumes that the strain increment of rocks can be decomposed into elastic strain increment  $e_i^e$  and plastic strain increment  $e_i^p$ , shown as follows:

$$\Delta e_i = \Delta e_i^e + \Delta e_i^p (i = 1, 2, 3) \tag{8}$$

For the elastic strain increment according to Hook’s law, the expression for elastic strain increment is:

$$\begin{aligned} \Delta \sigma_1 &= E \Delta e_1^e + \gamma (\Delta e_2^e + \Delta e_3^e) \\ \Delta \sigma_2 &= E \Delta e_2^e + \gamma (\Delta e_1^e + \Delta e_3^e) \\ \Delta \sigma_3 &= E \Delta e_3^e + \gamma (\Delta e_1^e + \Delta e_2^e) \end{aligned} \tag{9}$$

For the plastic strain increment, the Mohr–Coulomb condition is:

$$\begin{aligned}\tau &= c + \sigma_n \tan \phi \\ \frac{\sigma_1 - \sigma_3}{2} &= c \cos \phi + \frac{\sigma_1 + \sigma_3}{2} \sin \phi\end{aligned}\quad (10)$$

In the Formula (10),  $c$  is the cohesion force;  $\phi$  is the internal friction angle;  $\Delta\sigma_n$  is the normal stress on the shear plane.

(2) Initial stress field. The initial stress field test has not been carried out in this iron mine. Considering that the ore body is not deeply buried and tectonic stress is simple, the initial stress field selected in this calculation is only considered as the gravity stress field. The Mohr–Coulomb yield equation is:

$$\begin{aligned}f &= \sigma_1 - \sigma_3 N_\phi + 2c \sqrt{N_\phi} \\ N_\phi &= \frac{1 + \sin \phi}{1 - \sin \phi}\end{aligned}\quad (11)$$

It is defined by non-relevant flow rules as follows:

$$g = \sigma_1 - \sigma_3 \frac{1 + \sin \phi}{1 - \sin \phi}\quad (12)$$

In the Formula (12),  $g$  is the plastic potential surface;  $\phi$  is the expansion angle.

(3) Reduction of mechanical parameters. Rock mass is a complex medium composed of a series of structural planes and structures cut by structural planes, which is quite different from rock. In the calculation and analysis, it is necessary to reduce the indoor mechanical test results. Based on the engineering geological survey, this reduction treatment adopts the empirical formula and relevant norms for the elastic modulus, Poisson ratio, compressive strength, tensile strength, cohesion, internal friction angle, etc., as follows:

They adopt the formula of M.Georgi:

$$C_m = [0.114e^{-0.48(i-2)} + 0.02]C_K\quad (13)$$

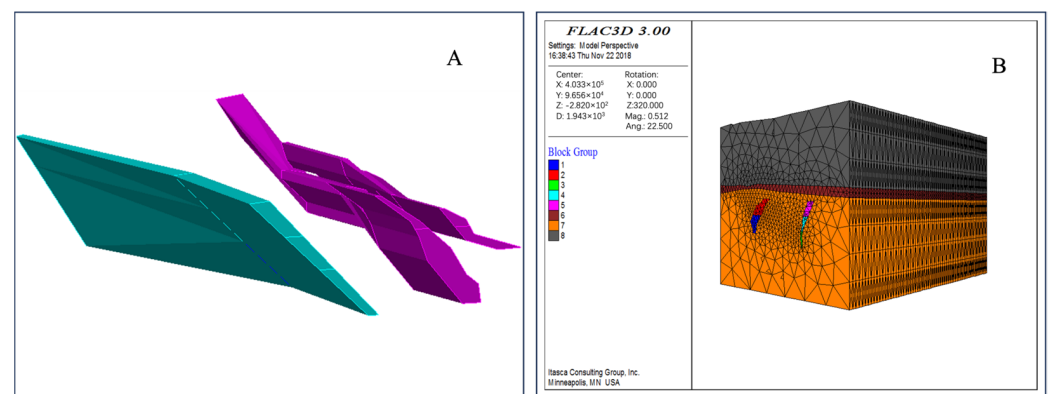
$i$ —Discontinuous plane density (bar/m), the value of which is referred to the survey results of ore-rock joints and fractures;  $C_K$ —Cohesion of rock (MPa);  $C_m$ —The cohesion of weakened rock mass (MPa).

According to the Code for Engineering Geological Investigation, the internal friction angle of rock mass is determined by the value of the internal friction angle of rock mass multiplied by the reduction coefficient determined according to the development degree of the rock mass. The fissure of the iron mine is relatively developed, and the reduction coefficient of the internal friction angle is 0.85. The modulus of elasticity is reduced. According to the Code for Design of Mine Roadway Engineering of Non-Ferrous Metal Mines, the elastic modulus of rock of 10%~20% is taken as the elastic modulus of rock mass, and 10% is taken this time. The cracking reduction coefficient was adopted for reduction. An elastic wave test was not conducted at this time. The cracking reduction coefficient  $K$  was calculated according to the degree of crack development and integrity of rock mass.

The reduced mechanical parameters are shown in Table 3. Based on the mining developing status, the backward mining from north to south is adopted in the horizontal direction, and the bottom-up mining sequence is adopted in the vertical direction to simulate the influence of ore body mining on the surface. Immediately after the stopping of the ore room, the cemented tailing filling is adopted to ensure that the top of the filling and the filling body reach the designed strength, and then the adjacent ore room is stopped, as shown in Figure 3.

**Table 3.** Summary table of physical and mechanical parameters of rock mass.

Lithology	Density (g/cm <sup>3</sup> )	Tensile Strength (MPa)	Compressive Strength (MPa)	Elasticity Modulus (GPa)	Poisson Ratio	Cohesion (MPa)	Internal Friction Angle (°)
Gneiss	2.79	2.47	48.60	5.08	0.26	1.98	38.05
Marble	2.72	3.34	59.80	6.77	0.32	3.39	37.40
Orebody	3.32	2.59	67.10	5.42	0.28	4.11	39.62
Weathered zone	2.41	16.56	0.41	1.62	0.28	1.08	31.05
Quaternary system	1.96	—	—	0.05	0.35	0.05	24
Fill object	1.90	0.25	1.68	0.9	0.30	0.67	29

**Figure 3.** The 3D solid model of orebody (A) and calculation model gridding (B).

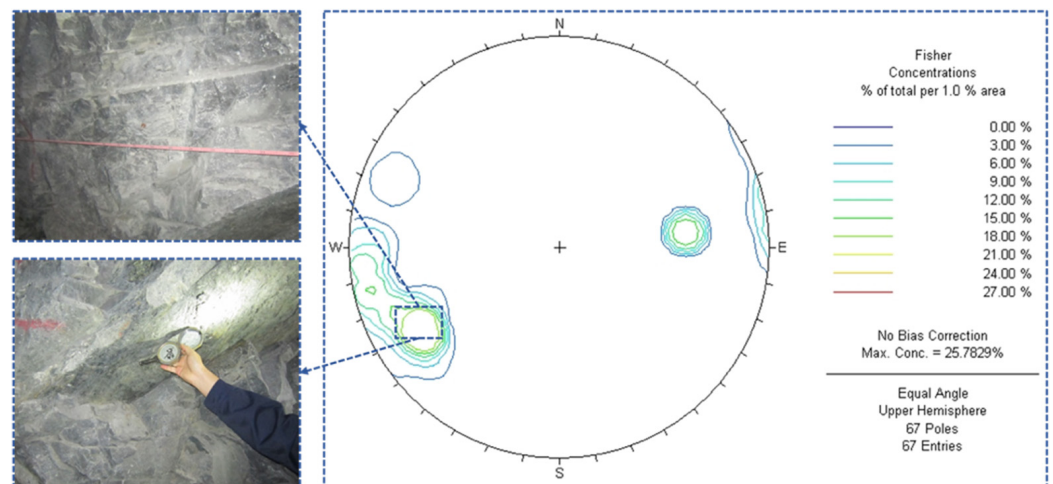
### 3. Results and Discussion

#### 3.1. Isodensity Map of Floor, Orebody, and Its Roof Joint Fissure Investigation

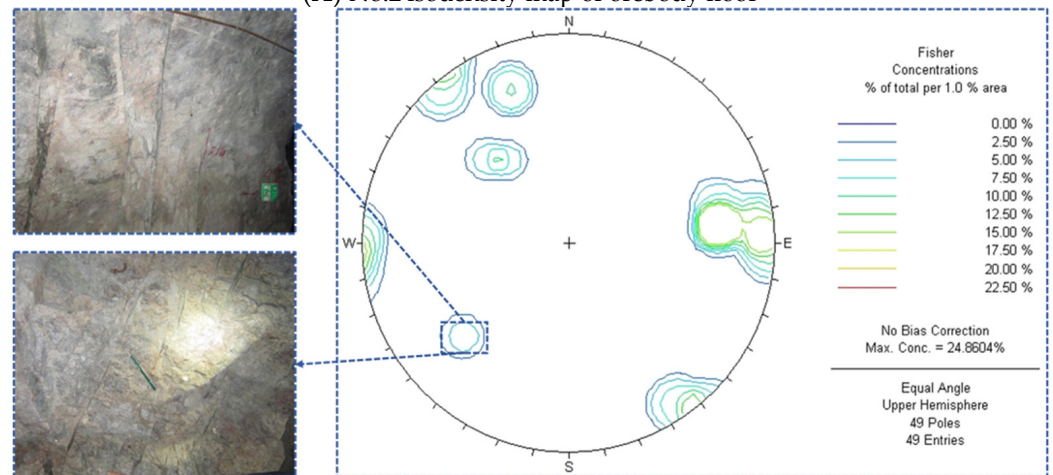
For the field investigation of II orebody floor, see Figure 4A for the isodensity of the orebody floor joint crack. Investigation area:  $-320$  m middle section of II mine footwall along vein roadway. The roadway azimuth is  $210^\circ$ , and the survey length is 17 m. The rock mass structure of this rock group is a massive structure, with only a few joints and fissures with good penetration. There are mainly two groups of joints, and the joints and cracks are mainly shear joints. The length of the structural plane trace line is 0.5–1 m, and the continuity is poor. The joint closure and quartz filling have a thickness of 0.5–2 cm, with good mechanical properties. The joint surface is straight and smooth, and the fracture surface is dry.

Figure 4B shows the isodensity diagram of the bottom joint crack of orebody II. Investigation area:  $-320$  m middle section II mine vein tunnel. The roadway azimuth is  $305^\circ$ , and the survey length is 11.4 m. The rock mass structure of this rock group is a massive structure, and there are two main groups of joints. The joint is more developed than that of the orebody floor, and the joint characteristics are the same as that of the orebody.

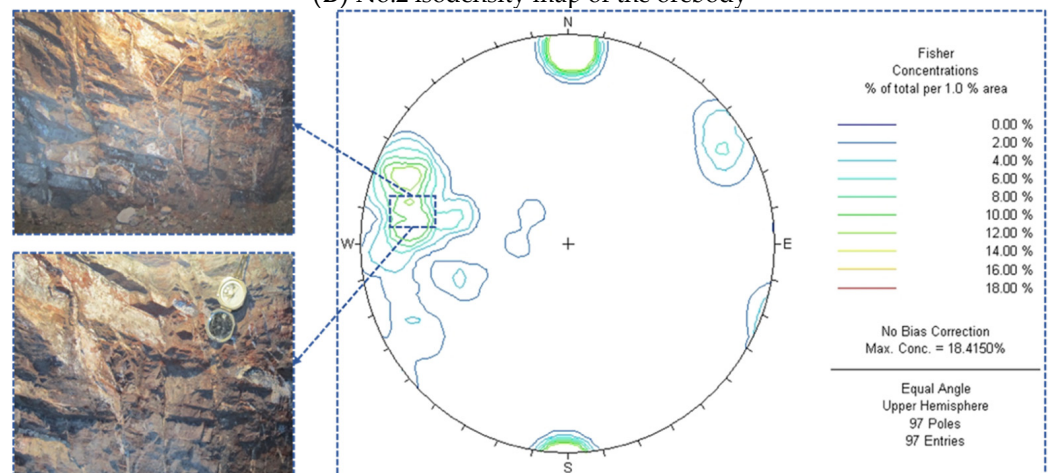
Figure 4C shows the isodensity diagram of the roof joint crack of orebody II. Investigation area:  $-320$  m middle section II mine upper wall along the vein roadway. The roadway azimuth is  $215^\circ$ , and the survey length is 17 m. The rock mass structure of this rock group is a massive structure, and there are two main groups of joints. The joints are more developed than the bottom and orebody of II orebody, and the length of the structural plane trace line is 0.5–1.5 m with poor continuity. The joint is closed, the joint surface is flat and smooth, and the fracture surface has a little water trace.



(A) No.2 isodensity map of orebody floor



(B) No.2 isodensity map of the orebody



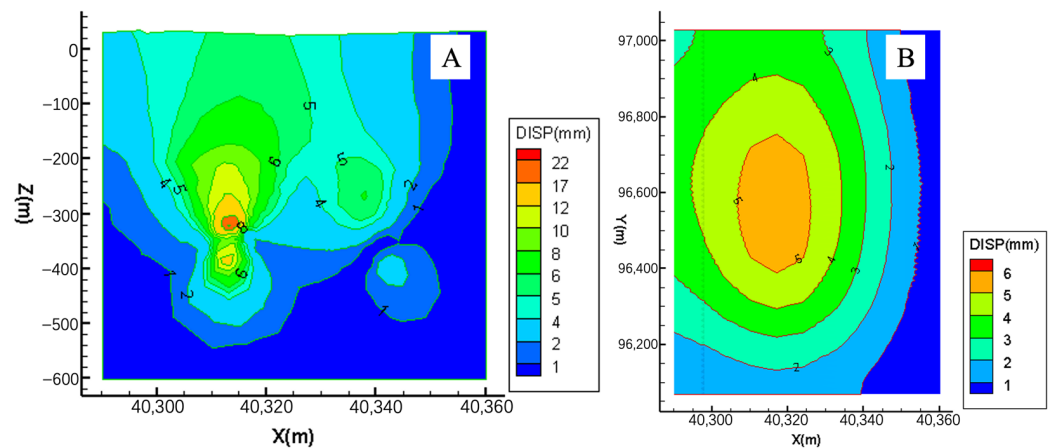
(C) No.2 isodensity map of the orebody roof

Figure 4. Isodensity map of joint fissure investigation in the floor (A), orebody (B), and roof (C).

### 3.2. Displacement Contour Map

#### (1) Displacement of mining status

Figure 5A shows the displacement contour map of line 1 of the mining status. After the mining of the ore body, the stress distribution state of the stope surrounding rock is disturbed, and the hanging wall and the roof and floor area of the ore body move towards the exposed surface due to the elastic recovery and the action of dead weight, resulting in the sinking of the hanging wall and the roof, and the heave of the footer and the floor. The maximum subsidence occurs in the middle area of the hanging wall of the ore body, with a maximum value of about 22 mm. The displacement away from this area gradually decreases, and the maximum surface displacement is 5 mm.



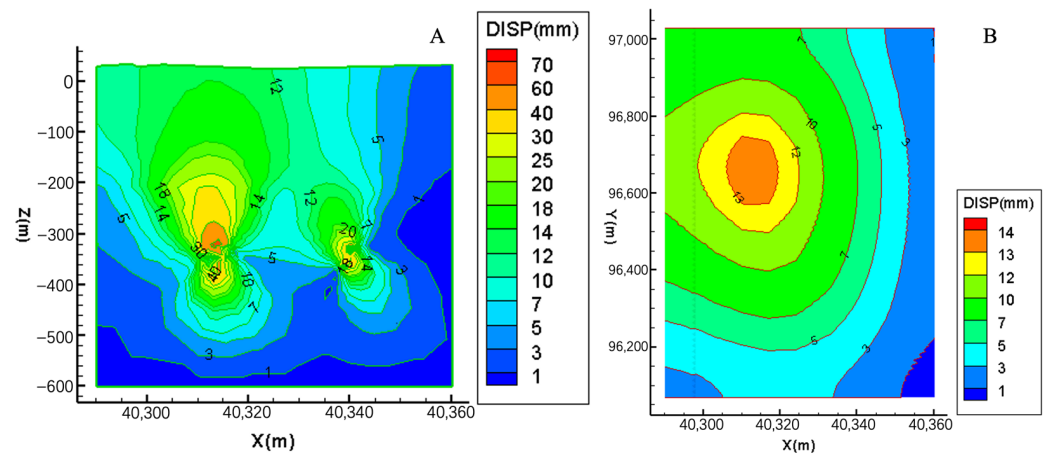
**Figure 5.** Mining status 1 displacement contour map of line (A) and surface (B).

The displacement isolines form a circle of contour line arches near the top and bottom floor of the goaf of the I and II orebodies, respectively. As the distance from the goaf floor increases, the arch diameter of the displacement isolines increases, the displacement value decreases gradually, and the surface develops into an unclosed contour line in the shape of a “funnel”. Because the stress release degree of the footwall area is smaller than that of the hanging wall, its displacement is slightly less affected by excavation disturbance than that of the hanging wall.

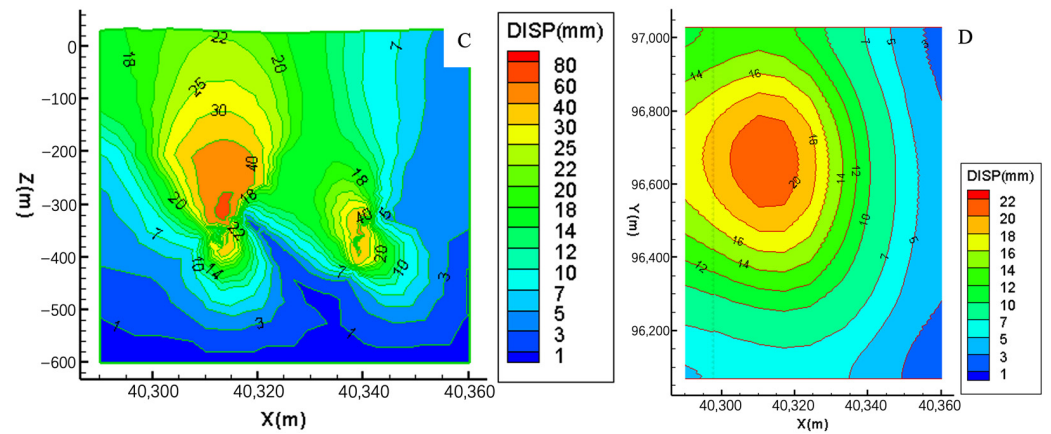
As can be seen from the surface displacement contour map of the mining situation in Figure 5B, the surface subsidence occurs under the influence of mining. The subsidence displacement is centered around the mining area and outwards presents a circle of contour line arches. The maximum surface settlement is 5 mm in the middle of the mining area. Away from the mining center, the arch diameter of the displacement contour line increases and the displacement value decreases gradually.

#### (2) Displacement of $-425$ m, $380$ m middle section and after mining

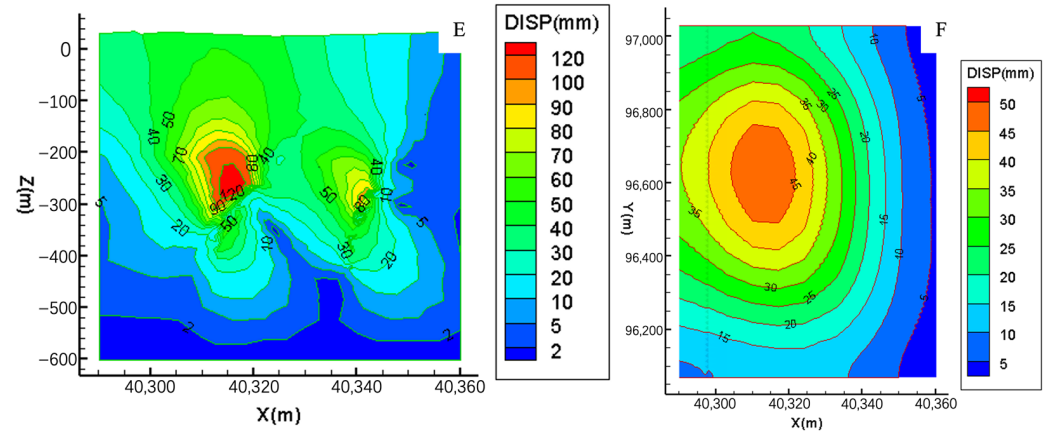
Figure 6A,B are the contour maps of line 1 and surface displacement after the end of mining in the middle section of  $-425$  m. It can be seen that the displacement increases with the increase of mining scope, and the maximum surface displacement is 13 mm. Figure 6C,D are the isographs of line 1 and surface displacement after the end of mining in the  $-380$  m middle section. After the end of mining in the  $-380$  m middle section, both surrounding rock and surface displacement increased steadily, and the maximum surface displacement increased to 20 mm. As can be seen from Figure 6E,F, line 1, and the surface displacement isograph after the mining end, as the mining range is close to the surface, the mining disturbance is obvious, and the surface displacement increases greatly. The maximum surface displacement is 45 mm.



(1) Displacement contour map of 1 line (A) and surface (B) of -425 m middle section



(2) Displacement contour map of 1 line (C) and surface (D) of -380 m middle section



(3) Displacement contour map of 1 line (E) and surface (F) of -380 m middle section

**Figure 6.** Displacement contour map of -425 m, 380 m middle section after mining.

### 3.3. Monitoring Point Transplantation, Surface Deformation and Curvature Calculation

In order to seek the maximum inclination, curvature, and horizontal deformation values of the mining surface, monitoring points are arranged in the areas where the surface displacement of the model changes obviously. Three monitoring points, Y1, Y2, and Y3, are arranged vertically, and three monitoring points, X1, X2, and X3, are arranged horizontally, as shown in Figure 7.

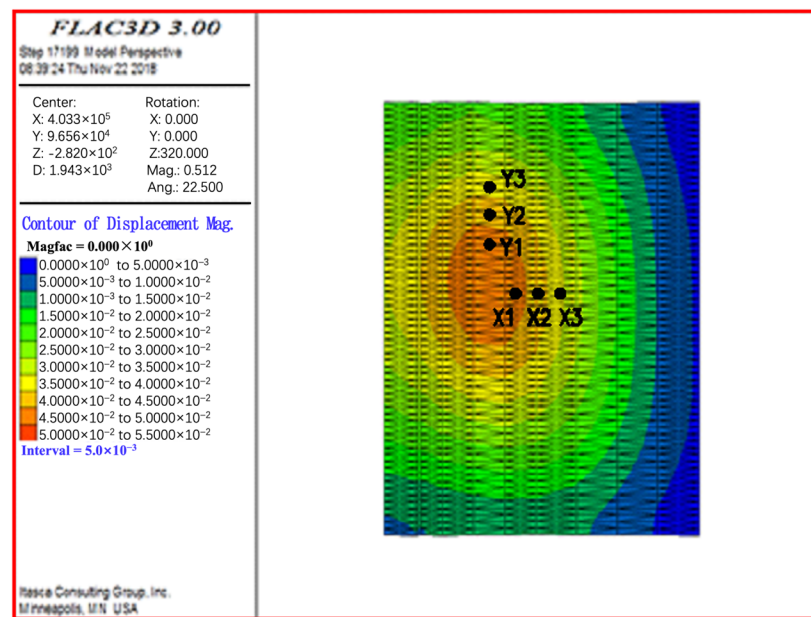


Figure 7. Layout of monitoring sites via Flac<sup>3D</sup>.

According to the horizontal displacement, vertical displacement, and the distance between each monitoring point, the corresponding tilt, curvature, and horizontal deformation values were calculated. The coordinates and vertical and horizontal displacements of each monitoring point are shown in Table 4. According to the calculation formula of deformation and curvature, the allowable value of deformation in the monitoring area was calculated by referring to the coordinates of the monitoring points vertical and horizontal displacement. The maximum tilt, curvature, and horizontal deformation of the monitoring area are 0.15 mm/m,  $0.004 \times 10^{-3}/m$ , and 0.045 mm/m, respectively (Table 5).

Table 4. Coordinates of each monitoring point, vertical and horizontal displacement values.

Node Numbering	Monitoring Point Coordinates			Vertical Displacement (mm)	Horizontal Displacement (mm)
	X	Y	Z		
Y1	403,100	96,750	31.85	51.86	7.51
Y2	403,100	96,810	31.86	45.23	5.46
Y3	403,100	96,870	31.86	35.72	2.78
X1	403,200	96,630	29.10	51.21	9.71
X2	403,250	96,630	26.35	40.26	8.07
X3	403,300	96,630	28.49	32.55	6.43

Table 5. Allowable deformation value of monitoring area.

Node No.	Horizontal Spacing (m)	Incline i (mm/m)	Curvature K ( $10^{-3}/m$ )	Horizontal Distortion $\epsilon$ (mm/m)
Y1	60.0	0.11	0.00083	0.034
Y2				
Y3				
X1	50.0	0.22	0.0014	0.033
X2				
X3				

#### 4. Conclusions

Combined with the mine geological data, preliminary scientific research work and design scheme, field investigation, and laboratory mechanical test, this paper discusses the effects of underground mining on surface and structure deformation. The empirical formula, numerical simulation, and field monitoring are used to demonstrate the influence of ore body mining on the deformation of structures. The conclusion is as follows:

The deformation of surface structures caused by the mining of iron ore will not affect its safety. According to the calculation formula of displacement and deformation, the maximum surface tilt of 0.15 mm/m, curvature of  $0.004 \times 10^{-3}/\text{m}$ , and horizontal deformation of 0.045 mm/m were calculated by placing monitoring points on the surface of the model. Far less than the allowable tilt deformation of 6 mm/m, curvature of  $0.4 \times 10^{-3}/\text{m}$ , and horizontal deformation of 4 mm/m.

According to the results of scientific research in the early stage of the mine, a 25 m thick roof pillar should be left below the weathering zone of the Fulaozhuang Iron mine. Combined with the mining range and mining sequence, FLAC3D software is used to simulate and calculate the influence of ore body mining on the surface. Through calculation: after the mining above  $-425$  m is finished, the maximum surface displacement accumulated is 45 mm.

Considering the calculation parameter selection of this study and the uncertainty of underground geological structure, and considering the risk factors existing in the Fulaozhuang Iron Mine, the following safety precautions should be taken in the mining process to ensure that the mining of ore body does not affect the safety of surface structures:

- ① Further strengthen the monitoring of surface subsidence;
- ② Multi-point feeding and sub-filling are adopted to ensure that stope filling is connected to the top;
- ③ Strengthen the exploration of the weathering zone, ensure that the upper part of the ore body is left with a 25 m thick roof pillar, and grouting is carried out on the weathering zone work hole to block the fissure water gushing channel.

**Author Contributions:** Conceptualization, P.L.; methodology, P.L. and L.W.; software, P.L.; validation, P.L.; data curation, P.L. and H.L.; writing—original draft preparation, P.L. and H.L.; writing—review and editing, L.W. and S.Y.; supervision, L.W.; project administration, L.W.; funding acquisition, L.W. and S.Y. All authors have read and agreed to the published version of the manuscript.

**Funding:** This research was funded by programs of Beijing Natural Science Foundation (2232080); National Natural Science Foundation of China (52374112, 52204124, 52034001); Postdoctoral Innovation Talents Support Program (BX20220036); Chinese Postdoctoral Science Foundation (2022M710356); Open project of the State Key Laboratory of Coal Mine resources and safety mining (SKLCRSM22KF006); State Key Laboratory of Safety and Health for Metal Mines (2021-JSKSSYS-01); and Fundamental Research Funds for the Central Universities (FRF-IDRY-21-010; QNXM20220001).

**Data Availability Statement:** The data are not publicly available due to confidential reasons.

**Acknowledgments:** Thanks for the great efforts of editors and reviewers.

**Conflicts of Interest:** Author Peizheng Liu, Leiming Wang were employed by the company Sinosteel Maanshan General Institute of Mining Research Co., Ltd. The remaining authors declare that the research was conducted in the absence of any commercial or financial relationships that could be construed as a potential conflict of interest.

#### References

1. Behera, A.; Rawat, K. A brief review paper on mining subsidence and its geo-environmental impact. *Mater. Today Proc.* **2023**. [CrossRef]
2. Altun, A.O.; Yilmaz, I.; Yildirim, M. A short review on the surficial impacts of underground mining. *Sci. Res. Essays* **2010**, *3*, 206–3212. Available online: <https://www.researchgate.net/publication/229044874> (accessed on 4 December 2021).
3. Monika; Govil, H.; Guha, S. Underground mine deformation monitoring using Synthetic Aperture Radar technique: A case study of Rajgamar coal mine of Korba Chhattisgarh, India. *J. Appl. Geophys.* **2023**, *209*, 104899. [CrossRef]

4. Wang, L.; Zhang, X.; Yin, S.; Zhang, X.; Liu, P.; Ilankoon, I.M.S.K. Three-dimensional characterisation of pore networks and fluid flow in segregated heaps in the presence of crushed ore and agglomerates. *Hydrometallurgy* **2023**, *219*, 106082. [[CrossRef](#)]
5. Cui, X.; Li, C.; Hu, Q.; Miao, X. Prediction of surface subsidence due to underground mining based on the zenith angle. *Int. J. Rock. Mech. Min.* **2013**, *60*, 246–252. [[CrossRef](#)]
6. Wang, L.; Yin, S.; Deng, B.; Wu, W. Copper sulfides leaching assisted by acidic seawater-based media: Ionic strength and mechanism. *Min. Eng.* **2022**, *175*, 107286. [[CrossRef](#)]
7. Li, W.; Gao, C.; Yin, X.; Li, J.; Qi, D.; Ren, J. A visco-elastic theoretical model for analysis of dynamic ground subsidence due to deep underground mining. *Appl. Math. Model.* **2015**, *39*, 5495–5506. [[CrossRef](#)]
8. Marschalko, M.; Yilmaz, I.; Bednárík, M.; Kubečka, K. Influence of underground mining activities on the slope deformation genesis: Doubrava Vrchovec, Doubrava Ujala and Staric case studies from Czech Republic. *Eng. Geol.* **2012**, *147*, 37–51. [[CrossRef](#)]
9. Marschalko, M.; Yilmaz, I.; Bednárík, M.; Kubečka, K. Deformation of slopes as a cause of underground mining activities: Three case studies from Ostrava–Karviná coal field (Czech Republic). *Environ. Monit. Assess.* **2012**, *184*, 6709–6733. [[CrossRef](#)] [[PubMed](#)]
10. Pan, R.; Li, Y.; Wang, H.; Chen, J.; Xu, Y.; Yang, H.; Cao, S. A new model for the identification of subcritical surface subsidence in deep pillarless mining. *Eng. Fail. Anal.* **2021**, *129*, 105631. [[CrossRef](#)]
11. Yang, D.; Qiu, H.; Ma, S.; Liu, Z.; Du, C.; Zhu, Y.; Cao, M. Slow surface subsidence and its impact on shallow loess landslides in a coal mining area. *Catena* **2022**, *209*, 105830. [[CrossRef](#)]
12. Li, X.; Wang, Y.; Hu, Y.; Zhou, C.; Zhang, H. Numerical investigation on stratum and surface deformation in underground phosphorite mining under different mining methods. *Front. Earth Sci.* **2022**, *10*, 831856. [[CrossRef](#)]
13. Xia, Y.; Wang, Y.; Du, S.; Liu, X.; Zhou, H. Integration of D-InSAR and GIS technology for identifying illegal underground mining in Yangquan District, Shanxi Province, China. *Environ. Earth Sci.* **2018**, *77*, 319. [[CrossRef](#)]
14. Li, P.; Yan, L.; Yao, D. Study of tunnel damage caused by underground mining deformation: Calculation, analysis, and reinforcement. *Adv. Civ. Eng.* **2019**, *2019*, 4865161. [[CrossRef](#)]
15. Zeng, Z.; Kou, X. Application of viscoelasticity to study the time-dependent surface subsidence caused by underground mining. *Eng. Geol.* **1992**, *32*, 279–284. [[CrossRef](#)]
16. Zhang, Z.; Mei, G.; Xu, N. A geometrically and locally adaptive remeshing method for finite difference modeling of mining-induced surface subsidence. *J. Rock. Mech. Geotech.* **2022**, *14*, 219–231. [[CrossRef](#)]
17. Sasaoka, T.; Takamoto, H.; Shimada, H.; Hamanaka, A.; Matsui, K. Surface subsidence due to underground mining operation under weak geological condition in Indonesia. *J. Rock. Mech. Geotech.* **2015**, *7*, 337–344. [[CrossRef](#)]
18. Zhao, X.; Yu, W.; Zhao, Y.; Fu, S. Numerical Estimation of Shaft Stability and Surface Deformation Induced by Underground Mining Transferred from Open-Pit Mining in Jinfeng Gold Mine. *Minerals* **2023**, *13*, 196. [[CrossRef](#)]
19. Brücker, C.; Preuße, A. The future of underground spatial planning and the resulting potential risks from the point of view of mining subsidence engineering. *Int. J. Min. Sci. Technol.* **2020**, *30*, 93–98. [[CrossRef](#)]
20. Wang, L.; Cheng, L.; Yin, S.; Zhang, X. Multiphase slurry flow regimes and its pipeline transportation of underground backfill in metal mine: Mini review. *Constr. Build. Mater.* **2023**, *402*, 133014. [[CrossRef](#)]

**Disclaimer/Publisher’s Note:** The statements, opinions and data contained in all publications are solely those of the individual author(s) and contributor(s) and not of MDPI and/or the editor(s). MDPI and/or the editor(s) disclaim responsibility for any injury to people or property resulting from any ideas, methods, instructions or products referred to in the content.